Supplementary Information and Figures

Stabilized real-time Brillouin microscopy reveals fractal organization of protein condensates in living cells

Claudia Testi[1]*, Emanuele Pontecorvo[1,2], Chiara Bartoli[1], Chiara Marzaro[1], Fabrizio Gala[1,2], Li Zhang[1], Giulia Zanini[1,2], Noemi d'Abbondanza[1], Maria Giovanna Garone[3], Valeria de Turris[1], Andrea Giuliani[4], Gaia di Timoteo[4], Irene Bozzoni[4], Alessandro Rosa[1,4] and Giancarlo Ruocco[1,5]

1: Center for Life Nano- and Neuro-Science, Istituto Italiano di Tecnologia, Rome, Italy
2: CrestOptics S.p.A., Rome, Italy
3: Stem Cell Medicine Department, Murdoch Children's Research Institute, Parkville, VIC, Australia
4: Department of Biology and Biotechnology Charles Darwin, Sapienza University of Rome, Rome, Italy
5: Dipartimento Di Fisica, Sapienza University of Rome, Rome, Italy.
**: corresponding author: claudia.testi@iit.it*

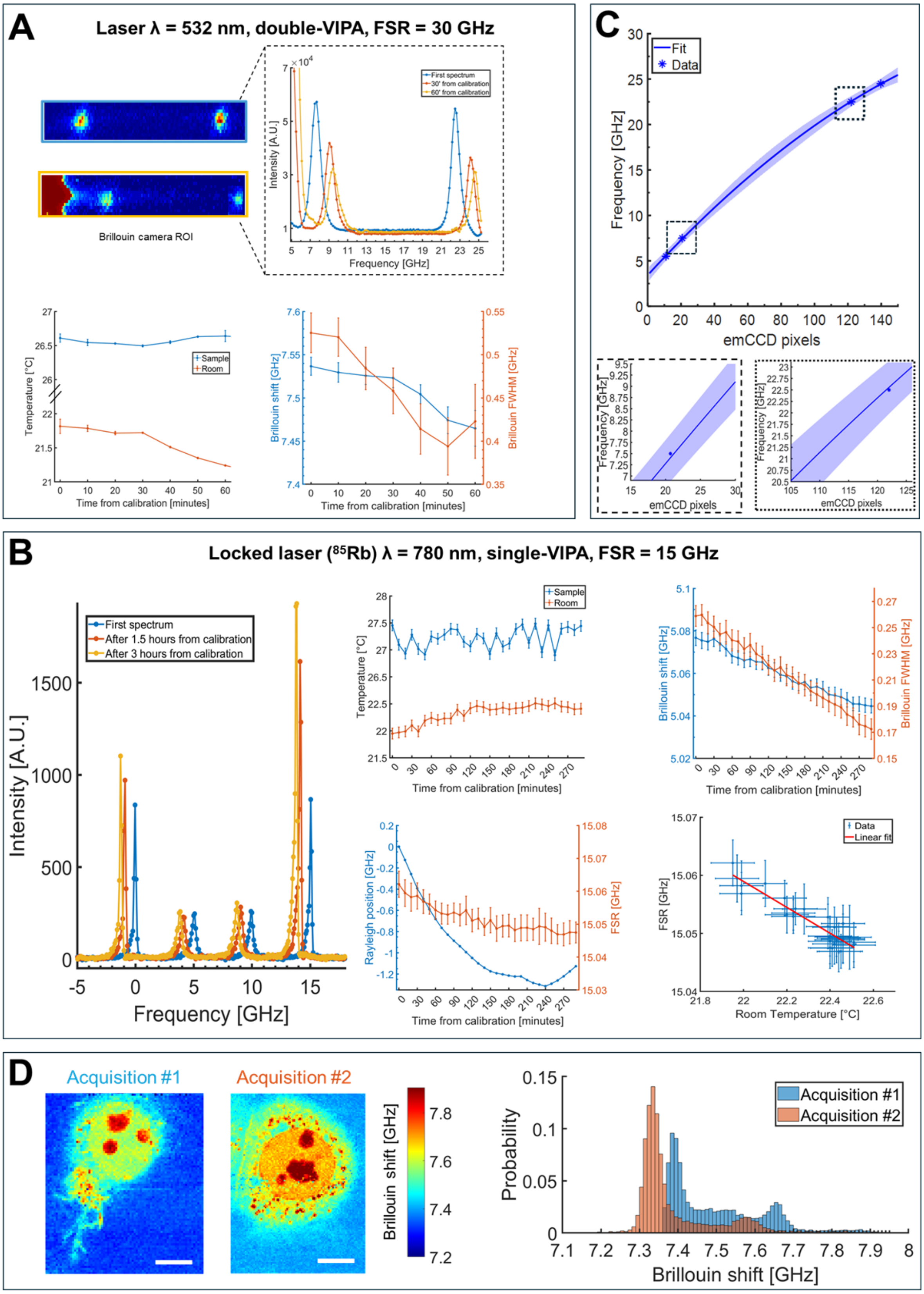

Supplementary Fig.1: Room temperature changes impact spectrometer stability of a standard BM, resulting in Brillouin spectra drifts during time. A: *Water data (kept at constant temperature with an incubator) acquired at different times with our 532 nm laser and double-VIPA setup (FSR=30 GHz). First graph: Brillouin water spectra acquired at different times: t=0 is the time at which spectrometer alignment and calibration have been performed, resulting in a Brillouin spectrum having 2 peaks of equal intensity (blue box and spectrum); because of small room temperature* *changes, this spectrum drifts in time, until camera saturation occurs as the parasitic Rayleigh line enters in the Brillouin camera ROI (yellow box and spectrum). Second graph: temperature recording of the room, showing small changes (<1°C) during time, and of the sample, that was kept in a temperature-controlled stage incubator. Third graph: behavior of water Brillouin shift v_B (blue data, changing ~1.06%) and linewidth Γ_B (red data): a Brillouin measurement was performed every 10'. Because of frequency drifts and spectral distortion, v_B and Γ_B changed in time although the sample temperature was kept constant.* ***B:*** *Water data (kept at constant temperature with an incubator) acquired at different times with a 780 nm laser, locked at ^{85}Rb, and a single-VIPA spectrometer (FSR=15 GHz). First panel: behavior in time of Brillouin spectra, showing the same drifts as in panel A; also here, t=0 is the time at which spectrometer alignment has been performed. Second panel: room and sample temperature behavior; the sample temperature was kept constant within a stage incubator. Third panel: observed changes in water v_B (blue data, varying by ~0.6%) and Γ_B (red data) are not caused by the sample, but are instead due to drifts in Rayleigh position and FSR (fourth panel, where FSR drifted by ~0.08%). Because of room temperature drifts, the Brillouin spectra, Rayleigh position and FSR all changed during time. Fifth panel: FSR was dependent from external room temperature changes (correlation coefficient = -0.93).* ***C:*** *Standard protocol for pixel-to-GHz calibration with water and methanol[20,23]. From their Brillouin spectra, we got 4 positions (blue stars in the plot): water at 7.5 GHz (Anti-Stokes) and 22.5 GHz (Stokes), methanol at 5.5 GHz (Anti-Stokes) and 24.5 GHz (Stokes), assuming a constant FSR = 30 GHz and Brillouin shifts values known from theoretical calculations. The continuous line represents the fit of the curve obtained with a 2nd order polynomial; shaded area is the 99% confidence interval. In the dotted boxes, close-up of the pixel-to-GHz calibration curve in the region of interest for biological applications, i.e. 7.5-9.5 GHz (7.5-8.1 GHz for cells with 532 nm illumination) and its Stokes counterpart.* ***D:*** *Brillouin maps of two fixed cells from the same population, acquired a few days apart with a standard 532 nm Brillouin Microscope. One might conclude that the cell #2 has a stiffer nucleus than cell #1, but this apparent difference is actually due to instrument-induced rigid translations. On the right, the distributions of v_B of both acquisitions clearly reveal this shift. This represents a common issue when imaging cells with a standard BM, where such artifacts can compromise data consistency and lead to misinterpretation of the results. Scale bars = 5 microns. (In panels A and B, all data are shown as mean ± standard deviation (SD) performed over 500 repeated measurements acquired at a single time; time = 0 refers to the manual alignment and calibration of the spectrometer, where Brillouin peaks have the same intensity).*

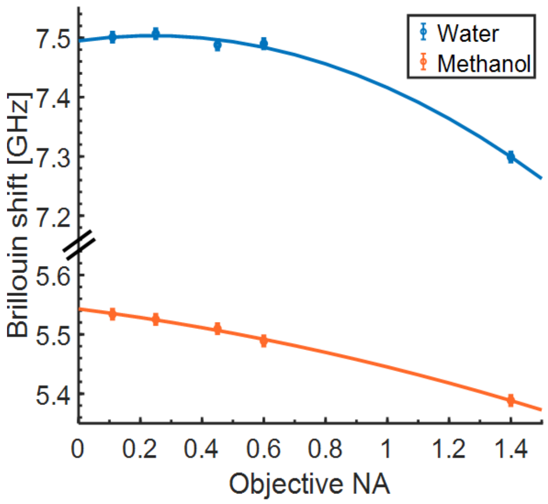

Supplementary Fig.2: Dependence of the Brillouin shift from the objective NA for the calibration materials. *Calibration materials as water (blue curve and data) and methanol (red curve and data) show a different dependence from the NA of the objective used[38]. Solid curves are 2nd order polynomial fit, used to extract the values of the Brillouin shift at NA = 0. The Brillouin shift values imposed in the pixel-to-GHz calibration that uses water and methanol as calibrators (shown in Supplementary Fig.1C and Figure 2C) are 7.50 GHz for water and 5.50 GHz for methanol: these have been extracted from theoretical considerations and are not true at high NAs. Data = mean ± SD performed on 500 measurements.*

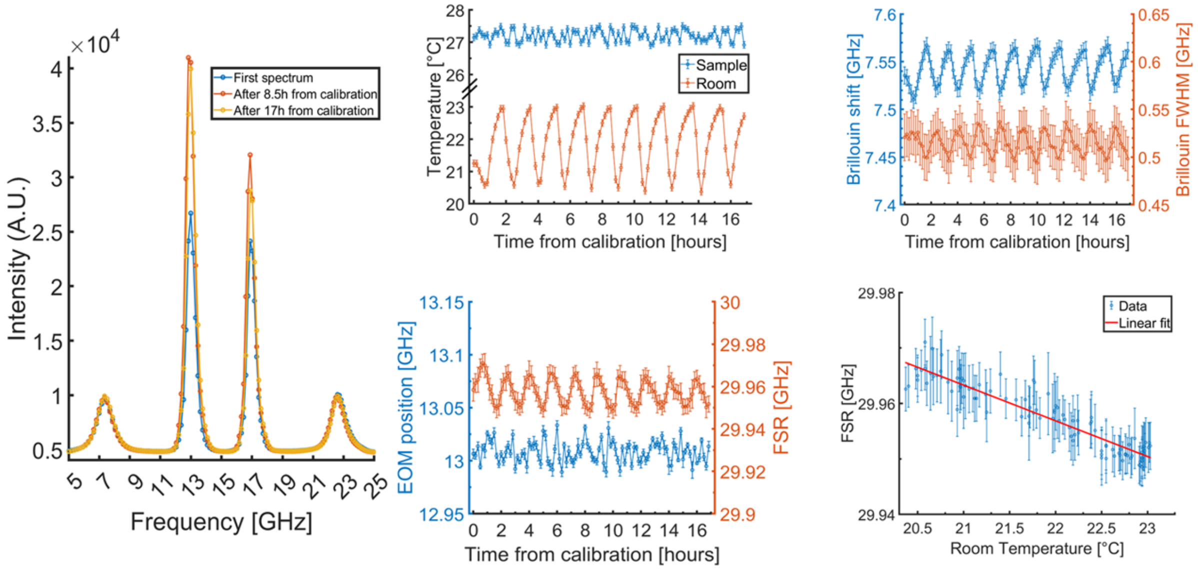

EOM-BM: EOM control loop, no recalibration in time

Supplementary Fig.3: The presence of the sole EOM-control loop is not sufficient to ensure spectrometer stability over time. *The temperature of water sample was kept constant through a top-stage incubator. These data were acquired using an active EOM-control loop (detailed in Figure 1C), but without applying the subsequent pixel-to-GHz recalibration of the spectrometer. We acquired Brillouin spectra of water every 10' for consecutive 17 hours. Thanks to the EOM control loop, the acquisition could continue without spectral distortion: Brillouin spectra did not show spectral drifts (first panel), thus no Rayleigh signal was detected, avoiding camera saturation. However, the presence of relatively big (~2.5°C) external room temperature drifts (second panel) caused periodic oscillations of Brillouin shift and FWHM in time (third panel; ν_B shifted ~0.8%). This happened because without recalibrations the FSR fluctuated in time (of about ~0.07%), while the EOM position remained stable (fourth panel). The FSR continued to be dependent on external room temperature (fifth panel, correlation coefficient = -0.93) as in other cases where no EOM-control loop was performed (as in Supplementary Fig.1B and Figure 3A). All data are shown as mean ± SD performed over 500 repeated measurements acquired at a single time; time = 0 refers to the manual alignment and calibration of the spectrometer, where Brillouin peaks have the same intensity.*

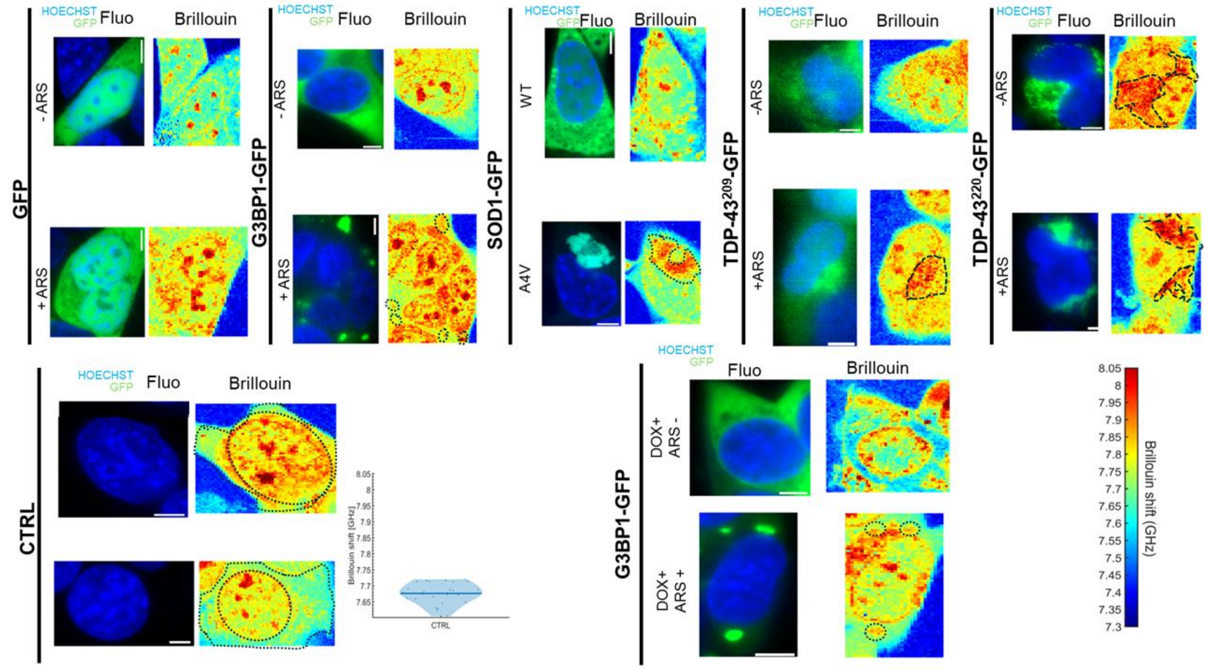

Supplementary Fig.4: additional Brillouin Microscopy maps on living SK-N-BE cells. *Dashed black contours highlight granules location in Brillouin maps, extracted from GFP fluorescence data. We also included Brillouin shift maps from control cells by extracting the Brillouin shift values of the pure cytoplasm, marked by dotted black contours. The average of these measurements was used to calculate the mean and standard error for cytoplasmic Brillouin shifts, represented in Figure 6 with the violet line and shaded areas. Scale bars = 5 µm.*

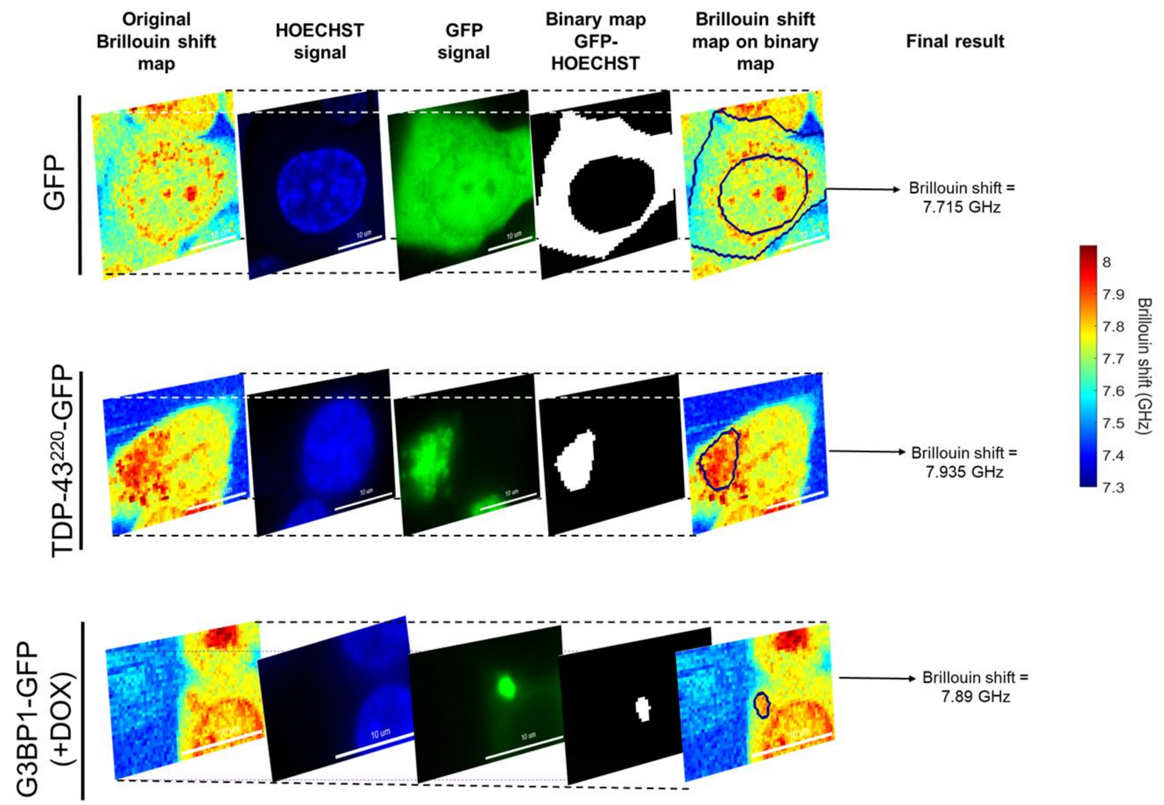

Supplementary Fig.5: post-processing analysis of Brillouin shift maps used to calculate mean Brillouin shift values. *We applied a binary map to the Brillouin shift map and calculated the mean over such area. The binary map was extracted from the GFP signal in the sole cytoplasm, obtained by subtracting the GFP to the HOECHST signal in case where the protein was expressed in both the cytoplasm and in the nuclei (as in GFP, upper panel) or consisting of the sole GFP signal in case where the protein was expressed only in the cytoplasm (as in TDP-43^{220}-GFP or G3BP1-GFP treated with doxycycline (DOX), lower panels). Scale bars = 10 µm.*

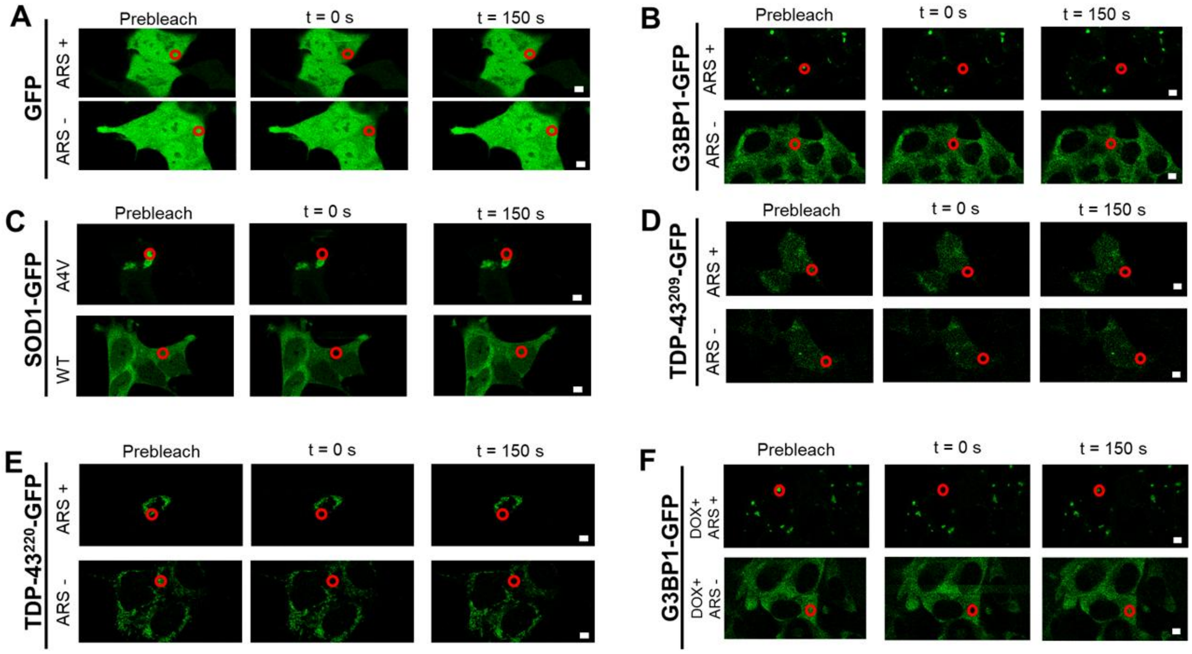

Supplementary Fig.6: representative FRAP images of all the condensates at different times. *In living cells, we photobleached a specific ROI (here shown as red circles) and then monitored its intensity recovery over time with custom-made MATLAB programs, thus producing FRAP curves of Figure 5C. ROIs diameters were fixed at 5.22 micron. Scale bars = 5 µm.*

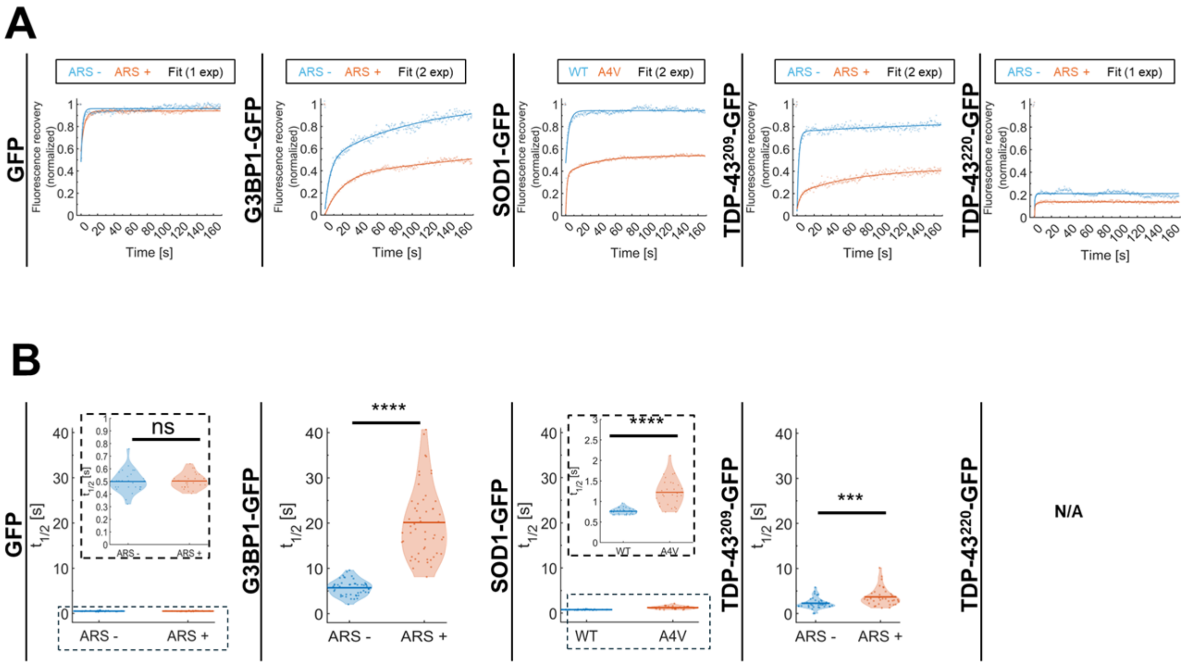

Supplementary Fig.7: FRAP curves fitting and half-recovery times. A: *representative FRAP curves from individual cells. These curves were fitted with custom-made MATLAB scripts by using non-linear least squares algorithms. Depending on the recovery behavior, we applied either single-exponential (for GFP, pure diffusion behavior, and TDP-43^{220}-GFP due of its limited fluorescence recovery) or double-exponential (for the others condensates, reflecting both diffusion and binding dynamics) models[21,75,76]. Raw data points are shown as dots and fitted curves are solid lines.* ***B:*** *half-recovery times extracted from the fit of the FRAP curves: their distribution is presented as violin plots. As for the immobile fractions, data were obtained from n=3 independent replicates (in every replicate, at least 10 cells were acquired). GFP: p=0.7, Wilcoxon runk-sum test; G3BP1-GFP: p=8*10^{-22}, t-test; SOD1-GFP: p=9*10^{-11}, Wilcoxon runk-sum test; TDP-43^{209}-GFP: p=2*10^{-4}, Wilcoxon runk-sum test. For TDP-43^{220}-GFP, $t_{1/2}$ could not be calculated due to the negligible recovery after photobleaching [7,21,75,76]. ns: not significative; ***: $p < 0.001$; ****: $p<0.0001$.*

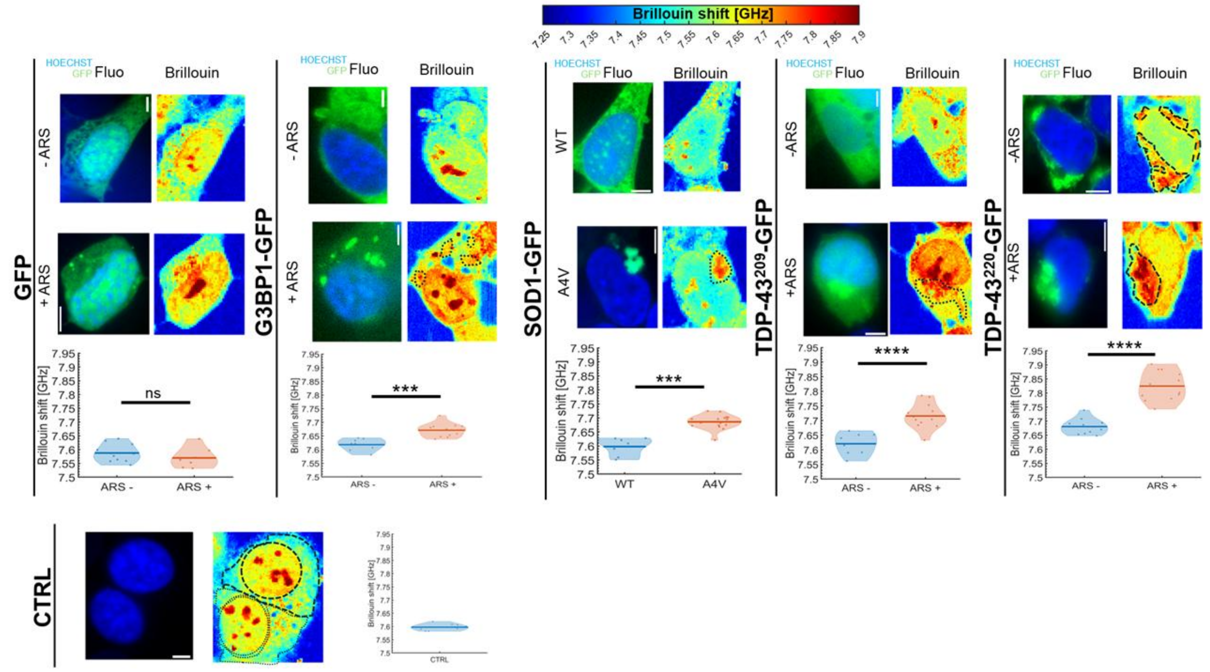

Supplementary Fig.8: Brillouin Microscopy measurements on fixed SK-N-BE cells. *Data were obtained from n≥2 independent biological replicates (in every replicate, at least 5 cells were acquired). In the lower panel, Brillouin maps acquired on control cells are shown to isolate the Brillouin shift distribution of pure cytoplasm, delineated by black dotted or dashed contours. Scale bars = 5 microns. GFP: p=0.3, Wilcoxon runk-sum test; G3BP1-GFP: p=2*10^{-4}, t-test; SOD1-GFP: p=5*10^{-7}, Wilcoxon runk-sum test; TDP-43^{209}-GFP: p= 8*10^{-5}, t-test; TDP-43^{220}-GFP: p=5*10^{-8}, t-test. ns: not significative; *: p < 0.05; ***: p<0.001; ****: p<0.0001.*

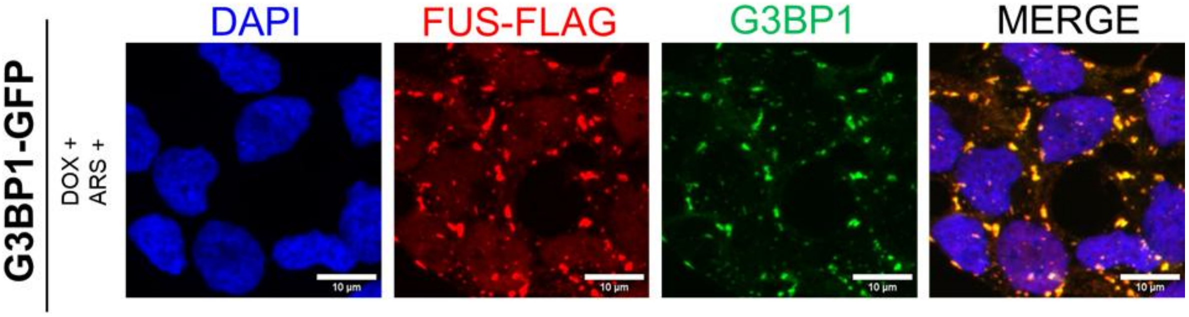

Supplementary Fig.9: immunofluorescence data on G3BP1-GFP cells treated with doxycycline and ARS show FUS^{P525L} presence inside G3BP1 granules. *Representative image upon DOX induction and 0.5mM ARS treatment for 1h. G3BP1 antibody staining is depicted in green, FUS-FLAG in red; cells nuclei are stained with DAPI (blue). The merge of the signal is shown. Scale bars = 10 µm.*

Supplementary Note 1

Our custom-built EOM-BM, equipped with a top stage incubator for temperature and CO_2 control, enabled biomechanical imaging of living SK-N-BE cells overexpressing several physiological and aberrant biomolecular condensates[2,4] in a physiological environment (Figure 5B & Supplementary Fig.4). Together with Brillouin maps, we simultaneously acquired brightfield and fluorescence images at the same focal plane.
FRAP data (Figure 5C, Supplementary Fig.6, Supplementary Fig.7) were obtained by monitoring the intensity of the photobleached region in time. Recovery curves of every condensate were fit to extract two parameters: the immobile fraction (Figure 5C, lower panels) and the half-recovery time (Supplementary Fig.7B).

Notably, we observed a strong correlation between Brillouin shifts (Figure 5B, lower panels) and FRAP immobile fractions (Figure 5C, lower panels) across the various condensates. In particular:
i) the GFP signal (non-fused to other proteins) exhibited a diffuse distribution throughout both the cytoplasm and nucleus, consistent with its known freely diffusive nature. GFP acted as an internal negative control for both Brillouin and FRAP: BM data revealed no significant changes in cells following ARS treatment (Figure 5B, first panel). The mechanical signature of GFP was indistinguishable from that of cytoplasm of non-transfected SK-N-BE control cells (shown in Supplementary Fig.4, lower panel), confirming its lack of phase separation. FRAP recovery curves displayed rapid and complete fluorescence recovery, indicative of diffusion-dominated dynamics: these curves were well-fitted by a single exponential model without binding[21] (Figure 5C, first panel; Supplementary Figures 7A & 7B), confirming GFP's liquid-like behavior under control and stressed conditions.
ii) G3BP1-GFP was evenly distributed in the cytoplasm; ARS treatment induced its condensation into discrete SGs foci in the cytoplasm[3,11,12]. BM detected a statistically significant increase in Brillouin shift upon SGs formation (Figure 5B, second panel), indicating a mechanical contrast between the condensates and the surrounding cytoplasm, in alignment with its fluorescence patterns. Coherently, the immobile fractions increased upon ARS release in cells (Figure 5C, second panel), consistent with the transition from a diffuse to a condensed state. These findings confirm that both BM and FRAP are sensitive to LLPS-driven transitions and are able to distinguish between a diffuse and a condensed protein.
iii) $SOD1^{WT}$–GFP exhibited diffuse cytoplasmic localization, while $SOD1^{A4V}$-GFP formed extended inclusions. In BM, such inclusions exhibited statistically significant higher Brillouin shift compared to the surrounding cytoplasm and co-localized with the fluorescence maps (Figure 5B, third panel). FRAP data of the $SOD1^{A4V}$-GFP condensates showed a significant reduction in mobility with respect to the WT (Figure 5C, third panel). These results suggest that $SOD1^{A4V}$-GFP aggregates possess increased stiffness and

reduced dynamics than the dispersed SOD1^{WT}–GFP, consistent with previous reports of their insoluble and toxic nature[50,58,68–70] and with the severe ALS phenotype of this mutation[56,57].

iv) TDP-43^{209}-GFP fluorescence signal in untreated cells showed heterogeneous cytoplasmic and nuclear localization. Brillouin shift maps revealed non-homogeneous mechanical stiffness in cytoplasmic regions, correlating with a partial reduction in FRAP mobility. ARS treatment significantly changed the cytoplasmic fluorescence distribution into condensates, having higher Brillouin shift (Figure 5B, fourth panel) and immobile fraction (Figure 5C, fourth panel; Supplementary Fig.6D). This is in line with stress-induced aggregation and cytotoxic behavior of this C-terminal fragment, purified from FTD brains, where oxidative stress is present[64,65,71–73].

v) TDP-43^{220}-GFP in absence of stress formed filamentous bundles inclusions in the cytoplasm, as in other reports[74]: these inclusions exhibited significantly higher Brillouin shifts than the surrounding cytoplasm, co-localizing with GFP fluorescence. Upon ARS exposure, the Brillouin shift increased further, suggesting enhanced condensation and rigidity (Figure 5B, fifth panel). Similarly, FRAP curves showed minimal fluorescence recovery in both cases, necessitating a pure-binding mono-exponential fit[7,21]. The immobile fraction of TDP-43^{220}–GFP was the highest among all condensates and further increased with stress (Figure 5C, fifth panel; Supplementary Fig.6E), indicating mechanical and dynamic impairment. These results are consistent with prior evidence of the aggregation-prone, insoluble, and toxic nature of this fragment[60–63,74] as well as its reduced cytoplasmic mobility under oxidative conditions in cells[67].

Taken together, these data show that higher Brillouin shifts, related to longitudinal elastic modulus, are associated with higher FRAP immobile fractions, defined as the portion of molecules that do not diffuse out of the bleached region after the recovery process. The immobile fraction parameter can be also related to the number of crosslinks formed within protein[81] and reflects the strength and extent of protein–protein, protein–RNA, and RNA–RNA interactions that maintain the granule's structure[2,3]. Thus, it is reasonable to identify FRAP immobile fractions with the number of occupied bonds in a protein network.

Putting together BM and FRAP data as in Figure 6, we observed a power-law relationship between Brillouin shifts and immobile fractions. This suggests that the mechanical response of the granules can be described by a gelation process (i.e. the phase transition from a liquid-like to a gel-like state), as occurs in aberrant SGs under stress[4,81]. Recent studies support this view, showing that biomolecular condensates such as SGs form and stabilize their internal architecture through a combination of liquid–liquid phase separation (LLPS) and a percolation-driven network transition[4,9,13,14,77–81]. Network percolation occurs when the concentration of binding sites among multivalent species exceeds a critical concentration (the percolation threshold, c_{perc}) defining the gel point[4,81] and encoded by the network of protein–protein, protein–RNA, and RNA–RNA interactions[3,11,12]. This network transition acts as a stabilizing mechanism in the internal structure of SGs[79–81] and ultimately governs its mechanical properties.

Gelation phenomena can be described using percolation models[82,88]. In a gelling system, the shear modulus G starts growing once the number of occupied bonds (x) surpasses a threshold x_0. Beyond this point, G increases following a power-law dependence on x, characteristic of percolating networks [82,88,89]:

$$G(x) - G_0 = \begin{cases} 0 & , \ x < x_0 \\ \alpha(x - x_0)^{\beta} & , \ x \geq x_0 \end{cases}$$

where x is the fraction of occupied bonds or sites, $x_0 \propto c_{perc}$ is the gelation threshold, α is a constant and β is an universal coefficient (from theoretical models describing the elastic properties of gelling systems such as polymers, β has been estimated[82] to be 1.95 in three dimensions).

On the other hand, the Brillouin shift is dependent on the longitudinal modulus M as[20,90]:

$$\nu_B = \frac{2n}{\lambda}\sqrt{\frac{M}{\rho}} = C\sqrt{M}$$

where C is a constant. The longitudinal modulus M is a combination[20,90] of K (bulk modulus) and G:

$$M = K + \frac{4}{3}G$$

In highly incompressible materials such as water (and likely biological matter like SGs), K is very large while G has a much smaller value[90]. We can thus rewrite the previous equation for ν_B as

$$\nu_B(x) = C\sqrt{K + \frac{4}{3}G(x)} \simeq C\sqrt{K}\left[1 + \frac{2}{3K}G(x)\right] = \begin{cases} \nu_0 & , \quad x < x_0 \\ \nu_0 + A(x - x_0)^{\beta} & , \quad x \geq x_0 \end{cases}$$

where A and ν_0 are appropriate constants.

Assuming that the fraction of the occupied bonds x is proportional to the immobile fraction obtained from FRAP data, we fitted Brillouin and FRAP data of Figure 6 with the above defined function for $\nu_B(x)$. This theoretical framework aligns well with our empirical findings, supporting the idea that SGs mechanics arise from an underlying network-based gelation process[4]. From a non-linear least squared fitting algorithm, we found the following parameters:

$x_0 = 0.04 \pm 0.2$

$A = (0.28 \pm 0.02)\ GHz$

$\beta = 2.0 \pm 0.2$

$$\nu_0 = (7.697 \pm 0.006)\ GHz$$

The retrieved value of ν_0 is consistent with the typical Brillouin shift of cytoplasm in living cells, found from control cells without condensates (seen in Supplementary Fig.4). The value of the exponential β is also consistent with the hypothesis of a gelling system undergoing a percolation transition[82]. This power-law behavior reinforces the idea that for concentrations higher that c_{perc} the diffusion dynamics of SGs is tightly linked to the fractal morphology of the percolating network of such condensates[15,79], as well as its viscoelastic properties.

This power-law behavior, moreover, suggest the hypothesis that the Brillouin shift behaves as the elastic modulus, contributing to the growing body of evidence in literature that the Brillouin shift is a reliable indicator of sample stiffness[20,91,92] and further validating its use for studying the phase separation of proteins in living cells.

Supplementary Note 2

After pointing out the capability of our EOM-BM in measuring the mechanical properties of physiological and aberrant molecular condensates in living cells, as shown in Figure 5, we wondered whether this technique could uncover intrinsic properties inaccessible to standard methods like FRAP.

Firstly, we validated BM results on the same cells after fixation (Supplementary Fig.8): here, the mechanical information of the condensates remained consistent to living cells with a rigid shift toward lower values in the fixed samples, coherently with previous reports indicating lower Brillouin shifts in fixed cells compared to living ones[93]. These data confirm that Brillouin microscopy yields comparable mechanical information for both living and fixed cells, and that cell fixation does not affect the mechanical properties of condensates. Consequently, this technique can be applied to study biomolecular condensates also in fixed samples, in contrast to FRAP[76]; this capability would be particularly valuable for mechanical characterizations of post-mortem tissues of ALS/FTD patients or for screening selective chemical compounds for their ability to disrupt pathogenic condensates.

Furthermore, we acquired an additional dataset of BM and FRAP on the same SK-N-BE cell line expressing G3BP1-GFP, this time in combination with a doxycycline-inducible mutant version of the Fused in Sarcoma (FUS) protein carrying the p.P525L pathogenic variant (associated with severe ALS[48]). Immunofluorescence data on these cells treated with doxycycline (DOX) and the oxidative stressor arsenite (ARS) confirmed that the overexpressed FUS^{P525L} co-localized with G3BP1-GFP into cytoplasmic SGs upon oxidative stress (as shown in Supplementary Fig.9[83]). We thus compared the effects of FUS^{P525L} presence on G3BP1-GFP granules, where the GFP tag enabled the visualization of the sole G3BP1 protein.

Resulting FRAP curves of DOX-treated G3BP1-GFP cells with or without ARS stress (Figure 7A; Supplementary Fig.6F) showed that immobile fractions and diffusion times increased after ARS treatment (yellow *vs* violet plots of Figure 7A). These curves displayed a temporal behavior similar to G3BP1-GFP alone: indeed, when comparing results between ARS-treated cells with or without DOX (orange *vs* violet plots), no significant differences were observed in immobile fractions or diffusion times, as highlighted by the red bars in Figure 7A. This result suggests that FUS^{P525L} did not modify G3BP1-GFP mobility, consistent with previous observations[94]: thus, while G3BP1 and FUS^{P525L} localize to the same compartment, they likely do not interact.

We then analyzed the same cells with our EOM-BM (Figure 7B). The presence of G3BP1-GFP granules upon ARS treatment was confirmed by fluorescence microscopy, and a binary mask was applied to average the Brillouin shift signals from these regions (Supplementary Fig.5, last panel). In DOX-treated cells (yellow *vs* violet plots), ARS treatment increased the Brillouin shift of G3BP1-GFP. In ARS-treated cells (orange *vs* violet plots), Brillouin shifts of G3BP1-GFP condensates containing FUS^{P525L} were significantly higher than those with G3BP1-GFP alone, as highlighted by red bars and asterisks of Figure 7B. This finding possibly suggests that FUS^{P525L} increased the stiffness of the granules, thus representing a substantial difference with FRAP data.

This difference might be attributed to the label-free nature of BM, which enables sensitivity to the overall stiffness of the SGs, influenced not only by G3BP1 but also by FUS^{P525L}, RNA and other RNA-binding proteins[5]. These data thus suggest that, in FRAP, the dependency from a fluorescent tag restricts the analysis to G3BP1-GFP as the sole measured component, not influenced by FUS^{P525L}. In contrast, BM post-processing analysis (shown in Supplementary Fig.5) uses G3BP1-GFP fluorescent signal only as a marker to localize the condensates, where FUS^{P525L} is present as well, while the actual Brillouin measurement pertains to the mechanical properties of the entire local compartment rather than merely the tagged protein. These findings suggest that FUS^{P525L} could consequently play a critical role in determining the mechanical properties of G3BP1 aggregates, efficiently detected by our EOM-BM but undistinguishable for FRAP.

Taken together, these data support the use of EOM-BM as a unique tool for studying phase separation of proteins in living cells. Its label-free nature enables mechanical characterization of protein condensates, offering distinct advantages over traditional methods like FRAP, such as: *i)* performing measurements on fixed samples, paving the way towards the mechanical characterization of post-mortem tissues; *ii)* obtaining spatially resolved maps of SGs mechanical properties inside living samples, and *iii)* studying SGs without prior knowledge of specific molecular components necessary for fluorescent tags.